SLAC-PUB-17434

Comprehensive comparison of two tracking codes for single-particle dynamics evaluation of a next-generation storage ring light source

Michael Borland,[1,*] Yipeng Sun,[1] and Xiaobiao Huang[2,†]

[1] *Argonne National Laboratory, 9700 Cass Avenue, Lemont, IL 60439*
[2] *SLAC National Accelerator Laboratory, 2575 Sand Hill Road, Menlo Park, CA, USA 94025*

(Dated: April 5, 2019)

Next-generation light sources based on the multi-bend achromat concept place great reliance on the accuracy of beam dynamics modeling. To ensure the success of such light sources, confirmation of design performance with at least two independent codes is prudent. The APS Upgrade (APS-U) lattice has been designed using the code `elegant`, which has existing and new features that are needed by the design. Corresponding, independent improvements have recently been made to Accelerator Toolbox (AT), in order to permit an independent check of nonlinear dynamics predictions. The new developments include the modeling of combined-function bending magnets with straight geometry and improved fringe field effects of quadrupole magnets. Calculations of linear and nonlinear lattice parameters and particle tracking results were compared, showing remarkable agreement was found between the two independently developed codes. This provides significant confirmation of the feasibility of the APS-U design.

I. INTRODUCTION

Accurate lattice modeling is of crucial importance in storage ring lattice designs. The successful operation of a storage ring requires a large dynamic aperture (DA) and large local momentum apertures (LMA) throughout the ring. During the design phase, these nonlinear beam dynamics measures are obtained through particle tracking with a lattice model. Presently a part of the standard design practice is to optimize the tracked DA and LMA with multi-objective optimizers using linear lattice parameters and nonlinear magnets as optimization decision variables [1–3]. Because the storage ring nonlinear beam dynamics depends on the linear and nonlinear lattice parameters in complex, subtle ways, small errors in the lattice model in either linear or nonlinear optics could potentially cause large errors in the DA and LMA predictions. Therefore, the validity of the multi-objective optimization results may strongly depend on the accuracy of the lattice model.

The requirement for high accuracy lattice modeling has increased substantially in recent years as many labs began pushing for the next generation, multi-bend-achromat (MBA) based storage ring light sources [4–6]. These new rings utilize much stronger quadrupole magnets to pack many more lattice cells over the circumference as compared to a traditional third generation storage ring. Chromaticity correction of such rings requires much stronger sextupoles, despite the adoption of the hybrid-MBA cell, a creative lattice configuration that reduces the sextupole strengths significantly [4]. The increase of the numbers and strengths of magnets makes it more important to model the individual magnet accurately since the errors from all magnets could add up to large errors in the nonlinear beam dynamics performance prediction.

The new lattice features of the next generation storage ring light sources, such as longitudinal gradient dipoles [7–11], combined-function bending magnets with strong quadrupole components, and negative bending [12, 13], call for new developments in the lattice codes. Combined-function bending magnets with straight geometry have been used in many third generation light sources. There have been a few studies on the lattice effects of such magnets [14–16]. But these studies have not yielded symplectic models that are usable in tracking codes. Fringe field effects are a major source of discrepancy between the lattice model and a real machine. Traditionally quadrupole magnets are often modeled as hard edge elements in lattice codes, although the impact of fringe fields to linear and nonlinear optics have been previously studied theoretically [17–20].

Because the success of next generation storage ring light source projects, such as the APS-U [5], relies heavily on lattice modeling, it is important to ensure the lattice modeling codes are implemented correctly. One way to check the validity of the codes is to benchmark against each other with lattice models that include all of the critical features. About 9 years ago, the storage ring light source community conducted an exercise to benchmark the codes that are commonly used for storage ring modeling [21]. A wide spread of results in both linear and nonlinear lattice parameters was found among the codes.

Recently we have implemented new features for `elegant` [22] and the Accelerator Toolbox (AT) [23] in separate, independent efforts. Afterwards we benchmarked the two codes using the APS-U lattice model and found very good agreement. In this paper we describe the new developments in both codes and the benchmarking results. We hope our effort will help the community to converge to a common lattice modeling practice. This paper is organized as follows. In Section II the new features of both codes are described. Section III presents the

* mborland@anl.gov
† xiahuang@slac.stanford.edu

This material is based upon work supported by the U.S. Department of Energy, Office of Science, under Contract No. DE-AC02-76SF00515.

various benchmarking results. The conclusion is given in Section IV.

II. NEW SINGLE PARTICLE DYNAMICS FEATURES

Over the years the `elegant` code has implemented many single particle dynamics features. To meet the lattice modeling needs for the APS-U project, recently several new features were added. The single particle dynamics features to be discussed here include the exact drift space, the quadrupole fringe field, and the combined-function dipole magnets with straight geometry. In order to provide an independent benchmark and provide further confidence in modeling of APS-U, the AT code has been recently updated to add some of these features. The new single particle dynamics features in `elegant` and AT are summarized in Table I.

A. Exact drift space

The Hamiltonian of particle motion in a drift space in canonical coordinates (x, p_x, y, p_y, z, δ) is given by

$$H = \sqrt{(1+\delta)^2 - p_x^2 - p_y^2} + (1+\delta). \tag{1}$$

Correspondingly, the map between the canonical coordinates at the entrance and exit faces of a drift space should be

$$x_1 = x_0 + \frac{p_{x0}L}{\sqrt{(1+\delta)^2 - p_{x0}^2 - p_{y0}^2}}, \qquad p_{x1} = p_{x0}, \tag{2}$$

$$y_1 = y_0 + \frac{p_{y0}L}{\sqrt{(1+\delta)^2 - p_{x0}^2 - p_{y0}^2}}, \qquad p_{y1} = p_{y0}, \tag{3}$$

$$z_1 = z_0 + \frac{(1+\delta)L}{\sqrt{(1+\delta)^2 - p_{x0}^2 - p_{y0}^2}} - L, \tag{4}$$

where subscripts 0 and 1 indicate the entrance and exit faces, respectively, and we have omitted $\delta_1 = \delta_0 = \delta$.

Tracking codes typically implement a simplified model for the drift space, using the Hamiltonian

$$H = \frac{p_x^2 + p_y^2}{2(1+\delta)}, \tag{5}$$

which is obtained from Eq. (1) by expanding the terms under the square root. The simplified model does not need to compute the square roots in the map. But it loses the higher order effects.

`elegant` has implemented the exact drift space through the element type `EDRIFT`. Elements that use the drift-kick-drift type symplectic integration in `elegant`, such as `KQUAD` and `KSEXT`, also implemented the exact drift space. AT has implemented the exact drift space with the pass method *LaDrift*. Its new fourth order symplectic integrator, *StrMPoleSymplectic4NPass*, uses the exact drift space, along with other features to be described below.

It turns out the conversion to exact drift space does not make a significant impact to the nonlinear beam dynamics behavior in the case of the APS-U lattice. For example, comparisons were performed using `elegant` of DA and LMA using exact and approximate drift-space implementations for the field-free regions (i.e., regions external to dipoles, quadrupoles, and sextupoles). No significant differences were seen.

B. Combined-function bending magnets with straight geometry

Combined-function dipole-quadrupole magnets are commonly used in storage ring light sources to save space and to modify the horizontal damping partition. If the magnet is built on a curved geometry that follows the reference trajectory of the ideal particle, it can be modeled as a sector dipole, with the fields expanded in curvilinear coordinates [24]. The linear motion can be described with a transfer matrix for which analytical expressions exist [25]. If higher order multipole components are involved, symplectic integration on the curved reference system can be performed. For example, in `elegant` this is performed using the `CSBEND` element, which uses the exact Hamiltonian and a fourth-order symplectic integrator.

However, some combined dipole-quadrupole magnets are built on a straight geometry, for reasons of mechanical simplicity and cost. In APS-U, two families of combined-function reverse bending magnets will have straight geometry. In this case, the field expansion used for a curved-pole magnet is incorrect. However, the magnetic field in the magnets can be given in very simple form using the Cartesian coordinates (X, Y, Z) by

$$B_Y = B_0 + B_1 X, \qquad B_X = B_1 Y. \tag{6}$$

In such a magnet, the reference trajectory is not an arc of a circle, since the bending field varies along the trajectory. The focusing gradient also varies with the beam trajectory as the component of the focusing gradient on the transverse plane will change with the s-coordinate. Therefore, this type of magnet cannot be described by the sector dipole model.

Modeling of a straight dipole magnet can be broken into three parts. First, at the entrance of the magnet, a coordinate transformation is performed to the Cartesian coordinates with one axis parallel to the axis of the magnet. Second, we must model the body of the magnet, for which, because of the potentially large values of the Cartesian coordinates, the exact Hamiltonian must be used. This is similar in principle to modeling of straight elements like quadrupoles and sextupoles using the exact Hamiltonian, something that has been standard in `elegant` for many years. Third, at the exit face an inverse transformation is performed to go back to the usual coordinates. This is similar to an approach proposed in Ref. [26] and was recently implemented in `elegant` [27], then AT.

While the implementations in `elegant` and AT are based on the same concepts, they were performed independently. For simplicity, we'll describe the AT implementation. We solve the beam motion through symplectic integration in the Cartesian coordinate system, using canonical coordinates (X, $X' = \frac{dX}{dZ}$, Y, $Y' = \frac{dY}{dZ}$, Δs, δ), where Δs is path length difference with the reference particle. At the entrance face, the coordinate transformation consists of three steps. First, the angle coordinates are found with

$$x' = \frac{dx}{ds} = \frac{p_x}{\sqrt{(1+\delta)^2 - p_x^2 - p_y^2}}, \tag{7a}$$

$$y' = \frac{dy}{ds} = \frac{p_y}{\sqrt{(1+\delta)^2 - p_x^2 - p_y^2}}. \tag{7b}$$

The particles are then propagated from the xy plane to the XY plane at the entrance point, which is followed by a rotation transformation to the Cartesian coordinates. The last two steps combined can be expressed as

$$X = \frac{x\cos\psi}{\cos(\frac{\theta}{2}+\psi)} + X_0, \tag{8a}$$

$$X' = \tan(\frac{\theta}{2}+\psi), \tag{8b}$$

$$Y' = \frac{y'}{\cos\frac{\theta}{2} - x'\sin\frac{\theta}{2}}, \tag{8c}$$

$$Y = y + xY'\sin\frac{\theta}{2}, \tag{8d}$$

$$\Delta s = \frac{x\tan\frac{\theta}{2}\sqrt{1+x'^2+y'^2}}{1 - x'\tan\frac{\theta}{2}}, \tag{8e}$$

where θ is the bending angle of the magnet, $\frac{\theta}{2}$ is assumed to be the entrance angle, $\psi = \tan^{-1} x'$, and X_0 is the X-coordinate for the reference orbit at the entrance point (where $Z = -\frac{L}{2}$, L is the straight length of the magnet). At the exit face, a similar transformation is performed. These transformations were previously used in AT for the pass method for direct integration of the equation of motion through arbitrary magnetic fields [15].

In both codes, the integration through the body of the rectangular magnet is done with the fourth order symplectic integrator, using drift and kick maps. The exact map for drift spaces has to be used in this case, given the large angle coordinates in the Cartesian coordinate system.

Unlike the case of a curvilinear dipole, the reference trajectory through a straight dipole must be determined numerically. Because the bending field in the magnet varies with the X-coordinate, the bending angle of a particle depends on the entrance point. The entrance point for the reference orbit, X_0, needs to be found numerically using the condition that the reference orbit is symmetric with a total bending angle of θ. However, this might result in a trajectory that is not centered in the magnet and so does not use the good field region. If in addition the magnetic field strength is varied (i.e., scaling B_0 and B_1 proportionally), the entrance point for the reference orbit will change. This gives us the freedom to set the reference orbit through the center of the good field region. This tuning procedure is implemented automatically in `elegant` and AT. When the magnetic field profile is available, from simulation or measurements, the current set point of the magnet should be determined according to the alignment requirement using a similar numeric procedure [14].

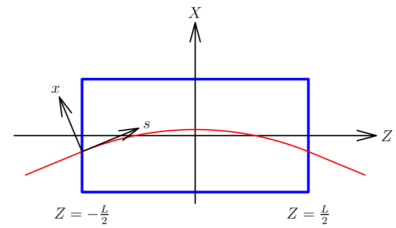

FIG. 1. Coordinates in a straight geometry combined-function dipole magnet.

C. Quadrupole fringe field

The magnetic field of a realistic quadrupole magnet extends beyond the iron core through a smooth transition curve at both edges, while in lattice models the magnet is typically described with a hard-edge field model in which the magnetic field drops to zero abruptly. The hard-edge model is not physically self-consistent, yet it has been remarkably successful in the past. For the new type of rings with more and stronger quadrupoles, the errors from the hard-edge model need to be properly accounted for. The linear optics error comes from the difference in the distribution of the focusing gradient between the real and the hard-edge profiles. This "soft fringe field" effect has been studied in Ref. [18] and later in more detail in Ref. [19]. There are also nonlinear effects from the quadrupole fringe field. [18, 20].

In AT the fringe field model in Ref. [18] was previously implemented for the transfer matrix based quadrupole pass method. Recently the more accurate model of Ref. [19] that was implemented in `elegant` was also implemented in AT, both for the transfer matrix based pass method and the straight element symplectic integrator. Suppose the difference of the focusing gradient profiles between the real and the hard-edge models is given by a function

$$\Delta K(s) = K(s) - K_h(s), \tag{9}$$

where $K(s)$ is the actual focusing gradient and $K_h(s)$

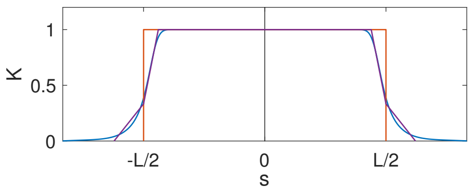

FIG. 2. Focusing gradient profile $K(s)$ for a realistic quadrupole magnet (blue) and the hard-edge model (red). The purple profile is the bilinear profile for testing the fringe field modeling approach.

is the focusing gradient for the corresponding hard-edge model. The function $K_h(s)$ is zero for $s < -s_0$ or $s > s_0$ and is equal to K_0 for $-s_0 \leq s \leq s_0$, where K_0 is the normalized gradient for the quadrupole, $s_0 = \frac{L}{2}$, and L is the effective length of the magnet. The fringe field model in Ref. [19] characterize the function $\Delta K(s)$ with a series of integrals for both the entrance and exit edges.

Fig. 2 shows an example of the focusing gradient profile of a real quadrupole magnet and its hard-edge model. The gradient of the hard-edge model is equal to the average gradient around the center of the magnet and the effective length is chosen to make the integrated gradient of the hard edge model equal to that of the real magnet. In both the `elegant` and AT implementations, the actual fringe field integrals as defined in Ref. [19] are supplied as parameters to the quadrupole element. At the entrance and exit edges, these integrals are used to modify the canonical coordinates according to the corresponding Hamiltonian terms.

The quadrupole fringe field modeling is checked with a bilinear test fringe field profile. In the test profile the gradient decreases to zero in two linear slopes, with a change of slope at the hard edge boundary, as illustrated in FIG. 2 (purple curve). Defining parameter Δ as the distance between the hard edge boundary to the starting point of the slope in the magnet, the fringe integrals for the bilinear profile are calculated to be

$$I_{0p} = -I_{0m} = \frac{1}{3}K_0\Delta, \tag{10a}$$

$$I_{1p} = 2I_{1m} = \frac{2}{9}K_0\Delta^2, \tag{10b}$$

$$I_{2p} = -4I_{1m} = \frac{2}{9}K_0\Delta^3, \tag{10c}$$

$$I_{2p} = 8I_{1m} = \frac{4}{15}K_0\Delta^4, \tag{10d}$$

$$\Lambda_2^+ = 2\Lambda_2^- = \frac{4}{135}K_0^2\Delta^3. \tag{10e}$$

The transfer matrix for the quadrupole magnet obtained with the quadrupole fringe field model can be compared to the one obtained by slicing the gradient profile into many pieces and concatenating the hard-edge transfer matrices of all pieces. In a numerical test, where $L = 1.0$ m, $\Delta = 0.1$ m, and $K_0 = 1.5$ m^{-2}, the differences between the the transfer matrices obtained with the two methods in the above are

$$\Delta R_x = \begin{pmatrix} 1.4 & -5.8 \\ -7.2 & 1.4 \end{pmatrix} \times 10^{-6}, \tag{11a}$$

$$\Delta R_y = \begin{pmatrix} -2.3 & -8.3 \\ -5.9 & -2.3 \end{pmatrix} \times 10^{-6}, \tag{11b}$$

while if using the hard-edge model without the quadrupole fringe field effect, the differences are

$$\Delta R_x = \begin{pmatrix} -0.0005 & 0.0079 \\ 0.0113 & -0.0005 \end{pmatrix}, \tag{12a}$$

$$\Delta R_y = \begin{pmatrix} -0.0008 & -0.0136 \\ 0.0181 & -0.0008 \end{pmatrix}, \tag{12b}$$

where $\Delta R_{x,y}$ are differences for the horizontal and vertical transfer matrices, respectively.

Additional numerical tests were performed with realistic fringe profiles and similar agreement between the fringe field model and the slicing approach was observed. In one test performed with `elegant` for one of the doublet magnets in the APS-U lattice, comparison was made to symplectic tracking through quadrupole fields defined by a generalized gradient expansion [28] computed from OPERA-generated field data. Such tracking is available using the `BGGEXP` element. Agreement in the linear matrix elements was within 2.5×10^{-7}, while agreement with the second-order matrix elements was within 5.0×10^{-4}. In performing this comparison, it was found to be essential to properly define $K(s)$ using the first term from the generalized gradient expansion, $2C_{2,s}^{(0)}(z)$. Analysis based on z-dependent harmonic analysis of the OPERA data showed much poorer agreement.

The leading terms in the nonlinear quadrupole fringe field effects for quadrupoles is the hard-edge map studied in Ref. [20]. The map for a normal quadrupole is not easy to implement in a tracking code since it is not a kick map. However, as pointed out in Ref. [20], the hard-edge nonlinear map of a skew quadrupole, whose generating function is given by

$$f = \frac{a_1}{6}(x^3 p_y + y^3 p_x), \quad a_1 = \frac{1}{B\rho}\frac{\partial B_x}{\partial x}, \tag{13}$$

is composed of two kick maps. Therefore, the map for a normal quadrupole can be modeled by first rotating the transverse coordinates of the particles by 45°, applying the two kicks, and then rotating backward by 45°. In AT, this is implemented at both edges of the element for the updated fourth order symplectic integrator pass method.

For the nonlinear effects, `elegant` uses the formulation of Lee-Whiting [29], which involves changes to position and momentum coordinates at the entrance and exit of the quadrupole. Higher order terms are also included [30], but these have a negligible effect on beam dynamics. As argued by Forest [26], the momentum kicks and position "jumps" are of comparable magnitude and should both be included, or else the map is "grossly non-symplectic." This implementation and the importance of

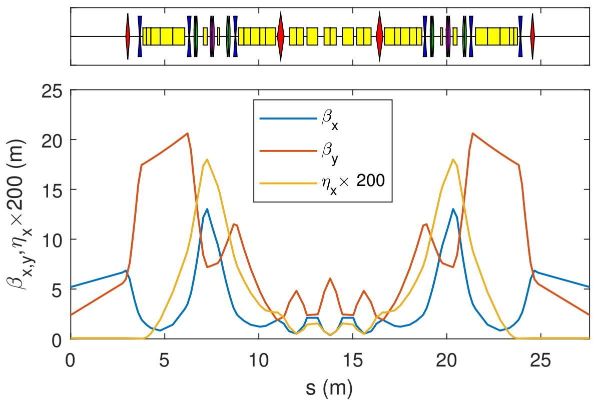

FIG. 3. Linear lattice functions for a sector of the APS-U lattice.

including both kicks and jumps was validated using comparison with the BGGEXP element to determine transport matrices up to third order by performing fits to tracking data[31]. We found that discrepancies in the third-order tracking-derived matrix were reduced by three orders of magnitude by inclusion of these terms. Removal of the position jumps significantly worsened the agreement.

III. COMPARISON BETWEEN THE TWO CODES WITH APS-U LATTICE

Comparison of the two codes, elegant and AT, was conducted as a way to validate the implementation of the modeling methods. We used the APS-U storage ring lattice as the test model. The APS-U lattice consists of 40 hybrid MBA cells over a circumference of 1103.6 m. The lattice cell contains 5 families of pure quadrupoles (Q1, Q2, Q3, Q6, and Q7), three families of combined-function sector dipoles (M3, M4 and Q8), two families of longitudinal gradient dipoles (M1 and M2), and two families of straight geometry combined-function dipoles (Q4 and Q5). Each family of magnets in the above has two magnets in one cell, which are symmetrically placed about the cell center, except for sector dipole M4 as it is located right at the center. There are six sextupoles in each cell, placed in reflection-symmetric locations of each cell in the high-dispersion regions. There are no harmonic sextpoles or powered octupoles, although provision for octupoles in dispersive and non-dispersive locations has been made. Instead, MOGA is used to adjust the sextupole strengths in 12 families, giving two-sector translational symmetry.

Magnets Q4, Q5, and Q8 provide negative bending, whereas M1, M2, M3, and M4 provide positive bending. The negative bending angle is 10.47% of the net bending angle. The natural emittance of the lattice is 41 pm for the 6-GeV ring. The beta and dispersion functions of one cell of the APS-U lattice is shown in Fig. 3.

In the following, the linear lattice parameters calculated with the two codes are compared first. This is followed by the tracking simulation of the dynamic aperture and the local momentum aperture.

A. Lattice parameters and linear optics

Table II lists a few lattice parameters. The betatron tunes are different by only -0.0007 and 0.0007 for the horizontal and vertical planes, respectively, out of the total tunes of $\nu_x = 95.1$ and $\nu_y = 36.1$. This is an indication of the level of agreement in the linear optics modeling between the two codes. The momentum compaction factor and the beam parameters (e.g., emittance, momentum spread) are all given by the linear topics and they have similar agreement. FIG. 4 shows the differences in a few linear optics functions between the two codes for one sector of the APS-U lattice. The fractional beta function difference, $\Delta\beta/\beta$, between the two codes is below 2×10^{-4} and the difference in dispersion function is below 1.5 μm.

The calculation of chromaticity is an area where simulation codes tend to disagree [21]. In our study, the natural chromaticities and the corrected chromaticities for the horizontal and vertical planes agree very well between elegant and AT. The natural chromaticities for the horizontal and vertical planes between AT and elegant differ by 0.06 and 0.16, out of -133 and -111, respectively. The small relative differences indicate that the modeling of energy dependence in focusing elements is consistent in the two codes. The differences in the corrected chromaticities are 0.05 and 0.15, respectively, which are nearly the same as the differences between the natural chromaticities. This is an indication that the energy dependence of particle motion in sextupole magnets is modeled consistently by the two codes, to a high degree of accuracy.

B. Nonlinear dynamics of the ideal lattice

The ability to reliably predict the nonlinear beam dynamics performance by simulation codes is a key requirement in the lattice design of next generation synchrotron light sources. Accurate modeling of nonlinear beam dynamics is more challenging than modeling the linear optics because the nonlinear beam motion can be very sensitive to the initial conditions of the particles. It is more important and relevant to benchmark the nonlinear dynamics predictions of the two simulation codes.

Because the betatron tunes differences between the two codes are very small, it is considered unnecessary to correct the betatron tunes in AT toward the elegant values before making comparisons for nonlinear beam dynamics predictions. It was found that making tune corrections with the Q1 and Q2 quadrupole families causes larger beta beats than the case without tune correction.

TABLE I. New single particle dynamics features in `elegant` and AT. (Note that the `KQUAD` and `KSEXT` elements have been standard in `elegant` for many years.)

Type	`elegant`	AT	comments
Drift	`EDRIFT`	LaDrift	exact drift space
Dipole	`CCBEND`	BndStrMPoleSymplectic4Pass	straight dipole
Quadrupole	`KQUAD`	StrMPoleSymplectic4NPass	w/ quadrupole fringe field
Sextupole	`KSEXT`	StrMPoleSymplectic4NPass	using exact drift

TABLE II. APS-U lattice parameters calculated with `elegant` and AT.

Parameter	`elegant`	AT
Horizontal tune, ν_x	95.0999	95.0993
Vertical tune, ν_y	36.0999	36.1007
Momentum compaction, $\times 10^{-5}$	4.0406	4.0399
Chromaticity, ξ_x	8.1183	8.1704
Chromaticity, ξ_y	4.7221	4.8739
Natural chrom., ξ_x^{nat}	-133.6488	-133.5874
Natural chrom., ξ_y^{nat}	-111.6335	-111.4689
Emittance (pm)	41.6612	41.6434
Energy loss per turn (MeV)	2.8688	2.8700
Momentum spread, σ_δ, $\times 10^{-3}$	1.3499	1.3494
Damping partition, J_x	2.2497	2.2495
Damping time τ_x (ms)	6.8446	6.8424

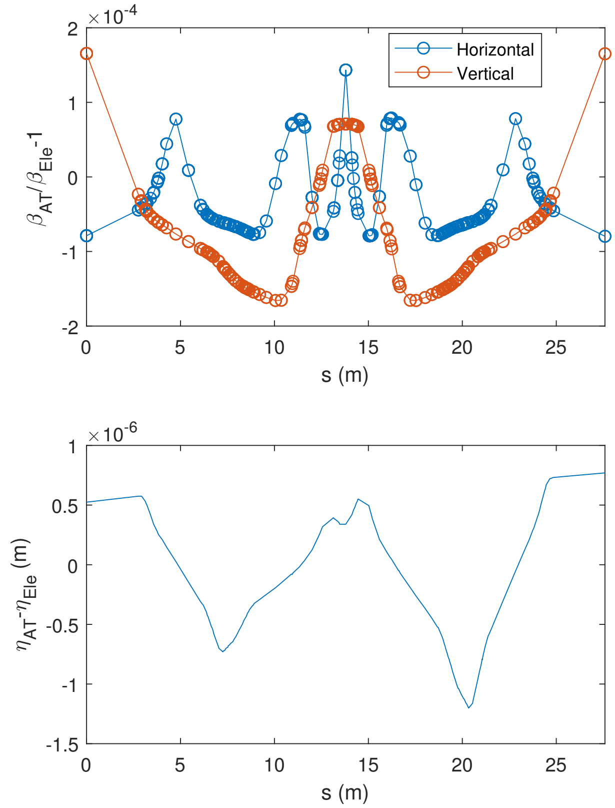

FIG. 4. Differences in linear optics functions between AT and `elegant` for a sector of the APS-U lattice. Top: fractional beta function difference; bottom: dispersion function.

We first compared the nonlinear dynamics behaviors predicted by the two codes for the ideal lattice. For this comparison, physical apertures are removed in the ideal lattice in order to allow modeling the particle motion at large oscillation amplitudes. In Fig. 5 the on-energy horizontal and vertical phase space profiles are compared between the two codes. Particles with an initial horizontal or vertical position offset are launched and tracked for 1024 turns. All other initial coordinates are set to zero. The RF cavity is turned off in this simulation. The phase space profiles traced out by the two codes are very similar, despite the severe distortion introduced by nonlinearity at large offsets. The largest horizontal and vertical contours in Fig. 5 correspond to the extent of the stable phase space area in the two transverse planes (while the action in the other plane is zero), respectively. The beta functions are $\beta_x = 5.20$ m and $\beta_y = 2.39$ m at the launching point. The island-like structures in the horizontal phase space plot by `elegant` indicate horizontal tune values that are very close to the low-order fraction numbers. The lack of such structures in the AT plot is due to the small tune difference of -0.0007.

Figure 6 compares the dynamic aperture (DA) of the ideal lattice determined by the two codes. Physical apertures, RF cavities, and radiation effects are all absent in the lattice model for this comparison. DA is determined by launching particles with initial position offset on the x-y plane and track for 1024 turns. The initial positions of the particles are on 19 rays extending from the origin. The DA boundary on each ray is given by the last surviving particle from the origin outward. The DA found by the two codes is nearly the same, except for small deviations in the upper right corner.

Frequency map analysis (FMA) [32] is also conducted for the ideal lattice. Particles on a dense grid in the x-y plane are tracked for 1024 turns. The tune diffusion, defined as the combined betatron tune shifts with time,

$$\text{diffusion} \equiv \log_{10} \sqrt{\Delta\nu_x^2 + \Delta\nu_y^2}, \tag{14}$$

is evaluated by computing the tune changes, $\Delta\nu_x$ and $\Delta\nu_y$, between the first and second 512 turns. Fig. 7 shows the comparison of tune diffusion rate in the tune diagram between AT and `elegant`. The tune footprint is nearly identical between the two codes. The differences in the diffusion seem to represent real differences between the two codes.

We also did FMA in the x-$\frac{\Delta p}{p}$ plane. The momentum

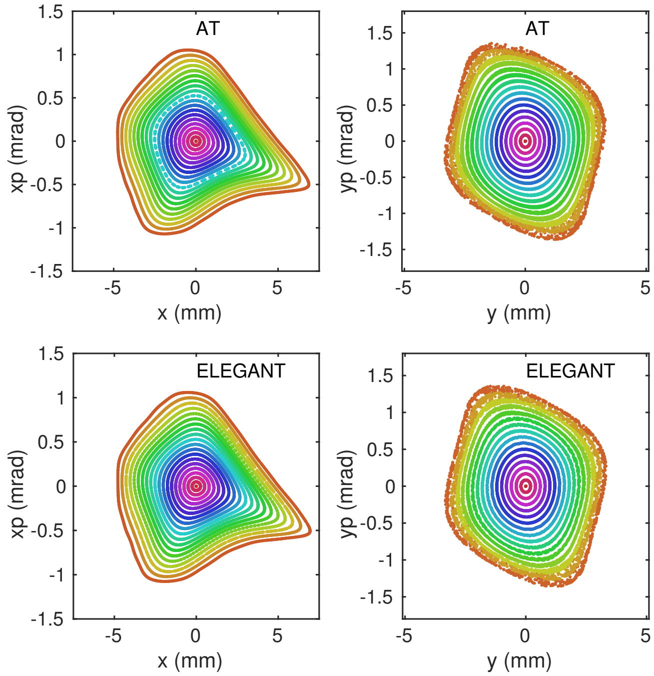

FIG. 5. Comparison of Hamiltonian contours in the horizontal phase space by tracking simulation for `elegant` and AT. $\beta_x = 5.20$ m and $\beta_y = 2.39$ m at the launching point. RF cavity is turned off in the model. Top: AT; bottom: `elegant`.

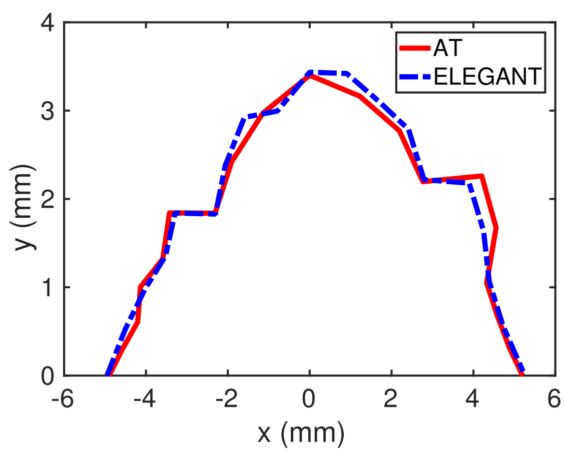

FIG. 6. Comparison of DA found by the two codes (`elegant` and AT) for the ideal APS-U lattice, without physical apertures, radiation, or RF cavity.

deviation coordinate is varied from -4.5% to 4.5% with the step size of 0.25%. Tune diffusion over the x-$\frac{\Delta p}{p}$ plane is plotted in Fig. 8. While again there is some difference in the evaluation of the tune diffusion, the stability region in the x-$\frac{\Delta p}{p}$ plane calculated by the two codes is very similar.

The dependence of betatron tunes over the momentum deviation is often used to characterize the off-energy dynamics performance of a lattice. Betatron tunes vs. momentum deviation for the APS-U lattice calculated by both codes are compared in Fig. 9. Within a large range of momentum errors, the tunes agree between the two codes to high accuracy. This indicates that the codes not only model the linear chromaticities in a consistent manner, but also the high order chromaticities.

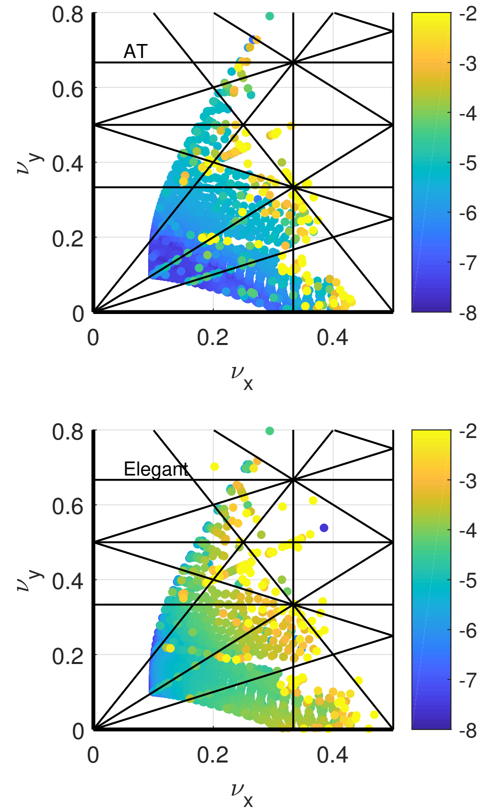

FIG. 7. Tune diagram for frequency map analysis in the x-y plane. The color code represents the detuning over 1024 turns, $\log_{10}(\sqrt{\Delta\nu_x^2 + \Delta\nu_y^2})$, where $\Delta\nu_x$ and $\Delta\nu_y$ are tune changes from the first 512 turns to the second 512 turns.

Comparison of the nonlinear beam dynamics performance for the APS-U upgrade lattice calculated by AT and `elegant` shows that the two codes are in very good agreement in the prediction of both geometric and chromatic behaviors within the full stability region of the lattice.

C. DA and LMA for lattices with linear errors

A workable lattice has to be able to deliver the required dynamic aperture and momentum aperture when a certain level of lattice errors is present because a realistic machine always has errors. The robustness of a lattice is typically checked by generating an ensemble of perturbed lattices, each with a different set of random errors, and evaluating the variation of DA and LMA among the ensemble. As a part of the code validation study, we

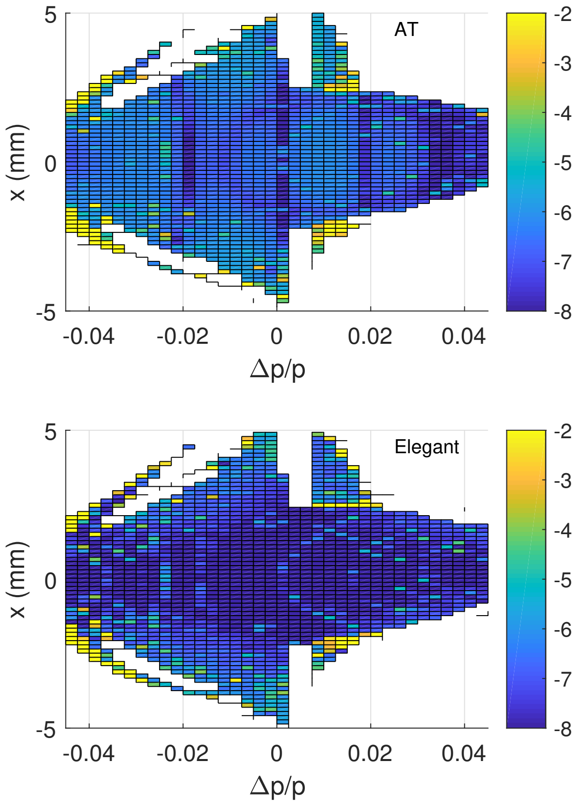

FIG. 8. Comparison of stability region in the x-$\frac{\Delta p}{p}$ plane as calculated by AT (top) or `elegant` (bottom). Color code represents tune diffusion as defined in Eq. (14).

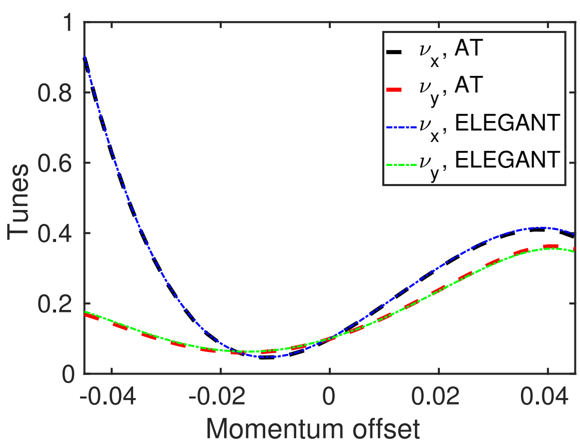

FIG. 9. Comparison of betatron tunes as a function of momentum deviation calculated by AT and `elegant`.

performed this process for the APS-U lattice with both AT and `elegant`.

We generated 25 perturbed lattices by introducing small random quadrupole and skew quadrupole errors to the sextupole magnets in the lattice. The level of quadrupole errors is chosen such that the horizontal and vertical beta beating (rms) are both on the order of 1%. The level of skew quadrupole errors give an emittance ratio of $\sim$ 10% when the horizontal and vertical tunes are shifted apart by 0.1 (with fractional part of ν_x and ν_y at 0.05 and 0.15, respectively). When the betatron tunes are restored, the ratio is $\sim$100%.

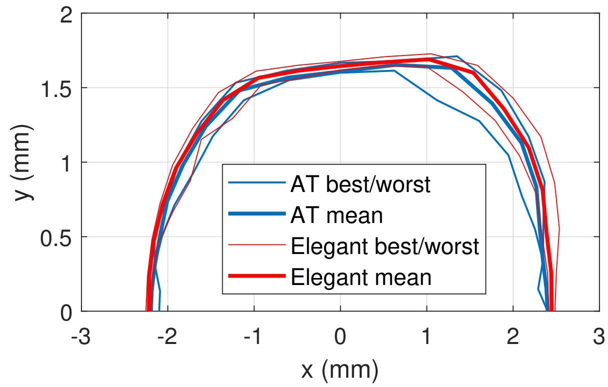

FIG. 10. Dynamic apertures with the same 25 error seeds evaluated by AT and `elegant` are compared. The think curves show the average DA of the 25 seeds, while the thin curves show the best and worst of all seeds. Tracking is done with physical apertures and radiation effects by bends. RF voltage is at 4.8 MV.

The DA and LMA are evaluated by particle tracking simulation in a realistic manner. The 352-MHz main RF cavities are turned on, with the total RF voltage set to 4.8 MV. Radiation damping is simulated by losing a proper amount of energy at each integration step in the dipole magnets for the particles. All the physical apertures are in the lattice model. The elliptic aperture passmethod is implemented in AT. A special aperture type, the "speed bump" aperture, is also implemented in AT using the same physics model as in `elegant` [33]; compared to a simple flat aperture, this method more accurately simulates the planned collimators in the high-dispersion region that are used to intercept Touschek-scattered particles.

The DA is determined by launching particles on 19 rays and tracking for 1024 turns as described earlier. The average DAs of the 25 lattices found by the two codes are plotted in FIG. 10 in thick curves. The best and worst DA among all lattices are shown with thin curves. There is good agreement except for a small difference at the upper right corner, which corresponds to the unstable region around $\nu_x = 0.2$ and $\nu_y = 0.2$ in FIG. 7.

The LMA is determined by launching particles with initial energy errors, ranging from $\delta = -0.06$ to 0.06, with step size of 0.0005 and tracking for 2048 turns from each location of interest. The locations of interest include the entrance and exit faces of all dipole magnets and the entrance points of all magnets in the first sector. FIG. 11 shows the distribution of LMA on the positive and negative sides over the length of the first sector for AT (top)

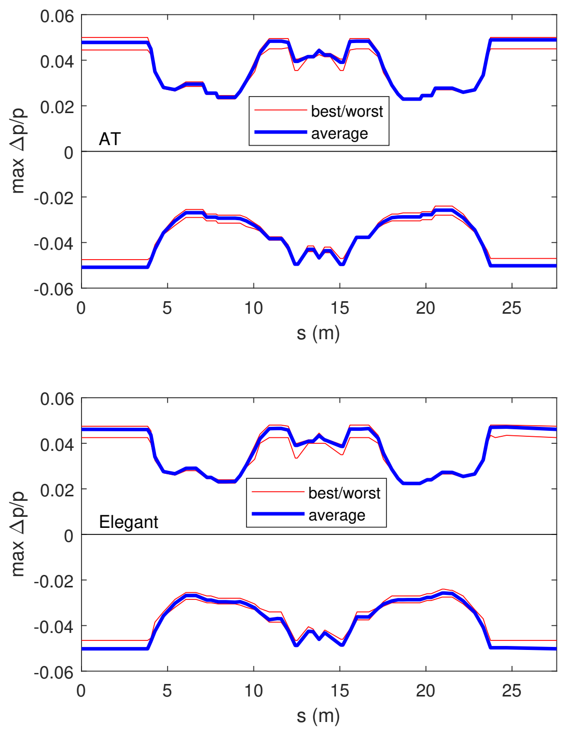

FIG. 11. Local momentum aperture for the first sector of the APS-U lattice with 25 random error seeds obtained with particle tracking by AT (top) or `elegant` (bottom).

and `elegant` (bottom). The results are remarkably close.

IV. CONCLUSION

In order to accurately model the nonlinear beam dynamics performance of next-generation storage ring light sources, new features were introduced into the lattice modeling codes `elegant` and AT in two separate, independent efforts. A new development in the codes is the proper modeling of combined-function quadrupole-bend magnets on a straight geometry. The linear and nonlinear effects of quadrupole fringe fields are also included in the lattice model. Quadrupole fringe field effects were previously modeled in `elegant` and AT; but typically they are not included in initial lattice designs.

We used the APS-U lattice to benchmark the two codes and found excellent agreement in both linear optics calculations and the prediction of nonlinear beam dynamics behaviors. The results we present here boost our confidence in making accurate predictions of lattice performance with precise modeling codes and encourage further refinement.

ACKNOWLEDGMENTS

This work was supported by the U.S. Department of Energy, Office of Science, Office of Basic Energy Sciences, under Contract No. DE-AC02-76SF00515 (SLAC) and under Contract No. W-31-109-ENG-38 (ANL).

[1] M. Borland, V. Sajaev, L. Emery, and A. Xiao, in *Proceedings of PAC 2009* (Vancouver, BC, Canada, 2009) pp. 3850–3852.
[2] L. Yang, Y. Li, W. Guo, and S. Krinsky, Phys. Rev. ST Accel. Beams **14**, 054001 (2011).
[3] X. Huang and J. Safranek, Nuclear Instruments and Methods in Physics Research Section A: Accelerators, Spectrometers, Detectors and Associated Equipment **757**, 48 (2014).
[4] L. Farvacque, N. Carmignani, J. Chavanne, A. Franchi, G. L. Bec, S. Liuzzo, B. Nash, and T. P. P. Raimondi, in *Proceedings of IPAC 2013*.
[5] "Advanced Photon Source Upgrade Project Preliminary Design Report, Argonne National Laboratory," (2017), aPSU-2.01-RPT-002.
[6] C. Steier *et al.*, in *Proceedings of IPAC 2015* (Richmond, VA, USA, 2015) pp. 1840–1842.
[7] J. Guo and T. Raubenheimer, in *Proceedings of EPAC02* (Paris, France, 2002) p. 1136.
[8] Y. Papaphilippou and P. Elleaume, in *Proceedings of PAC05* (Knoxville, TN, USA, 2005) p. 2086.
[9] R. Nagaoka and A. F. Wrulich, Nuclear Instruments and Methods in Physics Research Section A: Accelerators, Spectrometers, Detectors and Associated Equipment **575**, 292 (2007).
[10] C.-x. Wang, Phys. Rev. ST Accel. Beams **12**, 061001 (2009).
[11] A. Streun and A. Wrulich, Nuclear Instruments and Methods in Physics Research Section A: Accelerators, Spectrometers, Detectors and Associated Equipment **770**, 98 (2015).
[12] J. Delahaye and J. Potier, in *Proceedings of PAC89* (1989) p. 1611.
[13] A. Streun, Nuclear Instruments and Methods in Physics Research Section A: Accelerators, Spectrometers, Detectors and Associated Equipment **737**, 148 (2014).
[14] M. Yoon, J. Corbett, M. Cornacchia, J. Tanabe, and A. Terebilo, Nuclear Instruments and Methods in Physics Research Section A: Accelerators, Spectrometers, Detectors and Associated Equipment **523**, 9 (2004).
[15] X. Huang, J. Safranek, and D. Dell'Orco, in *Proceedings of IPAC10* (Kyoto, Japan, 4628) p. 4626.
[16] Y. Li and X. Huang, "A practical approach to extract symplectic transfer maps numerically for arbitrary magnetic elements," (2015), https://arxiv.org/pdf/1511.00710.pdf.
[17] G. E. Lee-Whiting, Nuclear Instruments and Methods **76**, 305 (1969).
[18] J. Irwin and C. x Wang, in *Proceedings of PAC95* (Dallas, Texas, 1995) pp. 2376–2378.
[19] D. Zhou, J. Tang, Y. Chen, and N. Wang, in *Proceedings of IPAC10* (Kyoto, Japan, 2010) pp. 4500–4502.

[20] E. Forest and J. Milutinovic, Nuclear Instruments and Methods in Physics Research Section A: Accelerators, Spectrometers, Detectors and Associated Equipment **269**, 474 (1988).

[21] D. Einfeld, "Summary of code comparison," `https://www.diamond.ac.uk/Home/Events/2009/NBD_workshop.html` (2009), nonlinear Beam Dynamics Workshop.

[22] M. Borland, "elegant: A flexible sdds-compliant code for accelerator simulation," (2000), advanced Photon Source LS-287, September 2000.

[23] A. Terebilo, in *Proceedings of PAC01* (Chicago, IL, 2001) pp. 3203–3205.

[24] L. C. Teng, *Expanded Form of Magnetic Field with Median Plane*, Tech. Rep. LCT-28 (ANL, 1962).

[25] K. L. Brown, *A First- and Second-Order Matrix Theory for the Design of Beam Transport Systems and Charged Particle Spectrometers*, Tech. Rep. 75 (SLAC, 1982).

[26] . Forest, *Beam Dynamics: A New Attitude and Framework*, The Physics and Technology of Particle and Photon Beams, Vol. 8 (Hardwood Academic / CRC Press, Amsterdam, The Netherlands, 1998).

[27] M. Borland, *Symplectic integration in elegant*, Tech. Rep. ANL/APS/LS-356 (Argonne National Laboratory, 2019).

[28] M. Venturini and A. J. Dragt, NIM A **427**, 387 (1999).

[29] G. E. Lee-Whiting, Nuclear Instruments and Methods **83**, 232 (1970).

[30] C. X. Wang, Private communication.

[31] M. Borland, *A High-Brightness Thermionic Microwave Electron Gun*, Tech. Rep. 402 (SLAC, 1991).

[32] J. Laskar, Physica D: Nonlinear Phenomena **67**, 257 (1993).

[33] "Elegant online manual," `https://ops.aps.anl.gov/manuals/elegant_latest/elegant.html`.